

Preclinical Evaluation of a Companion Diagnostic Radiopharmaceutical, [^{18}F]PSMA-1007, in a Subcutaneous Prostate Cancer Xenograft Mouse Model

Su Bin Kim, In Ho Song, Seon Yoo Kim, Hae Young Ko, Hee Seup Kil, Dae Yoon Chi, Frederik L. Giesel, Klaus Kopka, Alexander Hoepping, Joong-Hyun Chun, Hyun Soo Park,* Mijin Yun,* and Sang Eun Kim*



Cite This: *Mol. Pharmaceutics* 2023, 20, 1050–1060



Read Online

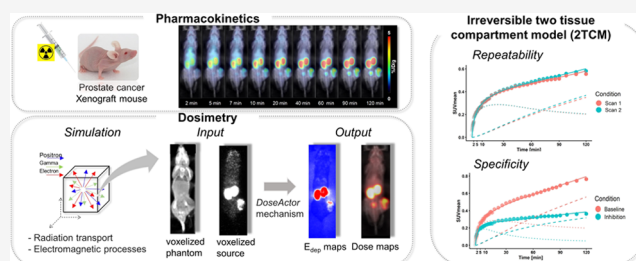
ACCESS |

Metrics & More

Article Recommendations

ABSTRACT: Several radiolabeled prostate-specific membrane antigen (PSMA)-targeted agents have been developed for detecting prostate cancer, using positron emission tomography imaging and targeted radionuclide therapy. Among them, [^{18}F]PSMA-1007 has several advantages, including a comparatively long half-life, delayed renal excretion, and compatible structure with α -/ β -particle emitter-labeled therapeutics. This study aimed to characterize the preclinical pharmacokinetics and internal radiation dosimetry of [^{18}F]PSMA-1007, as well as its repeatability and specificity for target binding using prostate tumor-bearing mice. In PSMA-positive tumor-bearing mice, the kidney showed the greatest accumulation of [^{18}F]PSMA-1007. The distribution in the tumor attained its peak concentration of 2.8%ID/g at 112 min after intravenous injection. The absorbed doses in the tumor and salivary glands were 0.079 ± 0.010 Gy/MBq and 0.036 ± 0.006 Gy/MBq, respectively. The variance of the net influx (K_i) of [^{18}F]PSMA-1007 to the tumor was minimal between scans performed in the same animals (within-subject coefficient of variation = 7.57%). [^{18}F]PSMA-1007 uptake in the tumor was specifically decreased by 32% in K_i after treatment with a PSMA inhibitor 2-(phosphonomethyl)-pentanedioic acid (2-PMPA). In the present study, we investigated the *in vivo* preclinical characteristics of [^{18}F]PSMA-1007. Our data from [^{18}F]PSMA-1007 PET/computed tomography (CT) studies in a subcutaneous prostate cancer xenograft mouse model supports clinical therapeutic strategies that use paired therapeutic radiopharmaceuticals (such as [^{177}Lu]Lu-PSMA-617), especially strategies with a quantitative radiation dose estimate for target lesions while minimizing radiation-induced toxicity to off-target tissues.

KEYWORDS: positron emission tomography, [^{18}F]PSMA-1007, internal radiation dosimetry, biodistribution, theranostics



INTRODUCTION

The recent development of small-molecule radiotracers targeting the prostate-specific membrane antigen (PSMA) has led to an exciting field of nuclear medicine called theranostics.¹ An ever-increasing number of PSMA tracers are being developed. In particular, ^{68}Ga - and ^{18}F -labeled PSMA radioligands show considerable potential to improve the diagnosis of prostate cancer. [^{68}Ga]Ga-PSMA-11 has been adopted for clinical use at several institutions worldwide and is the most widely used diagnostic radiopharmaceutical for positron emission tomography (PET) in clinical practice.^{2–5} However, the use of ^{68}Ga in labeling PSMA-targeting ligands is limited by its short half-life (68 min), the use of $^{68}\text{Ge}/^{68}\text{Ga}$ generators, and relatively high positron energy (1.90 MeV, 88.9% β^+), affecting the diagnostic accuracy in the small metastatic lesions required for adequate spatial resolution.⁶ Although the half-life of $^{68}\text{Ge}/^{68}\text{Ga}$ generators is 271 days, they

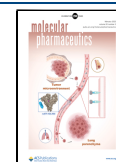
can offer a maximum activity of 1.85 GBq for ^{68}Ga , and they can only scan in a limited number of prostate cancer patients.⁷ For a higher number of patients in several PET centers with the characterization of ^{18}F , ^{18}F -labeled diagnostic radiopharmaceuticals targeting PSMA have several advantages.^{8,9} An on-site cyclotron produces large-scale ^{18}F without several productions, and ^{18}F has a longer half-life (109.8 min) and lower positron energy (0.65 MeV, 96.7% β^+), which increases the theoretical maximum spatial resolution.^{10,11}

Received: September 16, 2022

Revised: December 9, 2022

Accepted: December 12, 2022

Published: December 30, 2022



The recently developed [^{18}F]PSMA-1007 (((3S,10S,14S)-1-(4-(((S)-4-carboxy-2-((S)-4-carboxy-2-(6- ^{18}F -fluoronicotinamido)butanamido)butanamido)methyl)phenyl)-3-(naphthalen-2-ylmethyl)-1,4,12-trioxo-2,5,11,13-tetraazahexadecane-10,14,16-tricarboxylic acid)) is a promising companion diagnostic candidate for noninvasive PET imaging of prostate cancer and has been introduced in clinical practice.^{11–15} Compared to ^{68}Ga -labeled PSMA-11, which contains *N,N'*-bis[2-hydroxy-5-(ethylene-*b*-carboxy)benzyl]-ethylenediamine-*N,N'*-diacetic acid (HBED-CC) as the chelator, ^{18}F -labeled PSMA-radioligand has less hydrophilic glutamic acids with a high plasma protein binding affinity and the naphthalene-based linker region, which co-targets the hydrophobic accessory pocket.^{7,16} [^{18}F]PSMA-1007 is also being considered for using stable complexes with the trivalent therapeutic radionuclides ^{177}Lu , ^{90}Y , and ^{225}Ac and mimics the biodistribution behavior of labeled PSMA-617, showing predominantly hepatobiliary excretion,^{12,14} so is used in tandem with [^{177}Lu]Lu-PSMA-617.⁷

Preclinical evaluation of novel companion diagnostic or theranostic radiopharmaceuticals in disease/target-specific xenograft animal models is gaining interest because evidence-based clinical dose selection, dose–response relationships, and safety in terms of internal radiation dosimetry level must be translated before these radiopharmaceuticals can be implemented as personalized medicine and targeted radionuclide therapy (TRT) for patients.^{5,17,18} This study aimed to investigate the pharmacokinetic characteristics of [^{18}F]PSMA-1007 in a subcutaneous prostate cancer xenograft mouse model and estimate the internal radiation dosimetry for various organs, including tumors. Our findings support the clinical usefulness of [^{18}F]PSMA-1007 for use in personalized medicine and TRT in human cancer patients.

MATERIALS AND METHODS

Preparation of the Subcutaneous Prostate Cancer Xenograft Model. Male BALB/c mice (6 weeks old) were purchased from Orient Bio (South Korea). The mice were housed in a pathogen-free room maintained at $\sim 21\text{ }^{\circ}\text{C}$, $\sim 55\%$ relative humidity, and a 12 h light/dark cycle, with food and water available ad libitum. Feeding was limited prior to [^{18}F]PSMA-1007 PET/computed tomography (CT) imaging. A PSMA-positive human prostate carcinoma (LNCaP, Lymph node carcinoma of the prostate) cell line was purchased from Korea Cell Line Bank (South Korea) and maintained in RPMI 1640 medium containing 10% fetal bovine serum. LNCaP cells (1.0×10^7 cells in 200 μL phosphate-buffered saline) were inoculated subcutaneously into the right flank of the mouse. Finally, we prepared a total of 13 LNCaP tumor-bearing mice whose tumor sizes were measured using the formula: tumor size (cm^3) = (width (cm^2) \times length (cm))/2. The tumor sizes measured with calipers after inoculation and before imaging were $0.689 \pm 0.119\text{ cm}^3$, whereas the size measured by the imaging software after PET/CT imaging was $0.571 \pm 0.078\text{ cm}^3$. To avoid unnecessarily euthanizing experimental animals, eight mice were used in the biodistribution, internal radiation dosimetry, repeatability, and specificity studies, concomitantly. The remaining five mice were assigned to the inhibition group in the specificity study to evaluate the differences against the baseline group consisting of independent animals used in the prior studies.

All experimental procedures were approved by the Institutional Animal Care and Use Committee of Seoul National

University Bundang Hospital (no. BA-2002-291-021-02) and carried out in accordance with institutionally relevant guidelines and regulations. The study was performed in compliance with the ARRIVE guidelines.

Preparation of [^{18}F]PSMA-1007. The radiolabeling precursor (PSMA precursor, acetate salt) was obtained from ABX Advanced Biochemical Compounds (Radeberg, Germany).^{7,16} [^{18}F]PSMA-1007 was produced according to the known method by adapting solid-phase extraction (SPE) and high-performance liquid chromatography (HPLC) purification.¹⁹ In this study, the commercial sCUBE radiosynthesizer (FutureChem, South Korea) was used to produce [^{18}F]PSMA-1007 in high radiochemical yield (RCY) with the HPLC purification system. In detail, the tetrabutylammonium fluoride ([^{18}F]TBAF) was generated by eluting the ^{18}F anion-trapped quaternary methyl ammonium (QMA) cartridge with a solution of 1 M tetrabutylammonium hydrogen carbonate (TBAHCO₃, 800 μL) for ^{18}F labeling. The labeling reaction was carried out at 100 $^{\circ}\text{C}$, and the radiochemical conversion (RCC) of [^{18}F]PSMA-1007 was found to be higher than 88% from radio-thin-layer chromatography (TLC) determination. The purification of the reaction mixture was carried out by HPLC, using 30% acetonitrile/WFI in 0.1% trifluoroacetic acid (TFA) as a mobile phase under isocratic conditions. The product collected from HPLC was subsequently subjected to SPE purification through the tC18 Cartridge plus short (WAT036810, Waters, MA) to remove the residual solvent and the impurities. The final [^{18}F]PSMA-1007 was formulated in 10% ethanol/0.9% saline after Sep-Pak Purification. The overall synthesis time was approximately 55 min (including HPLC purification), and the isolated RCY was in the range of 30–32% ($n = 25$, non-decay-corrected). Quality control (QC) of [^{18}F]PSMA-1007 satisfied nine release criteria (i.e., appearance, identity, radiochemical purity, radionuclidic purity, chemical purity, pH, endotoxins, filter integrity, and sterility). All QC parameters were determined to be within the acceptable criteria, and there were no outstanding deviations.²⁰

In Vivo PET/CT Imaging Procedures. Basically, the animals underwent whole-body PET/CT scans twice using an animal-dedicated PET/CT system (NanoPET/CT, Mediso, Budapest, Hungary) with a 10 cm axial and 12 cm transaxial field of view (FOV). The PET spatial resolution was 1.2 mm full width at half-maximum at the center of FOV. A CT scan (semicircular full trajectory, maximum field of view, 480 projections, 50 kVp, 300 ms, and 1:4 binning) was performed immediately before the PET scan. In the biodistribution and internal radiation dosimetry studies, we acquired whole-body PET/CT images of the eight LNCaP tumor-bearing mice at 0–120 min (dynamic) post-injection of [^{18}F]PSMA-1007. The additional PET/CT scans were repeated 2 days after the first scan (Scan 1) using the same animals to add the second dataset (Scan 2) of PET/CT images for the repeatability analysis. The other five LNCaP tumor-bearing mice who were assigned to the inhibition group in the specificity study underwent 120 min dynamic whole-body PET/CT scans after treatment with the PSMA-selective inhibitor, 2-(phosphonomethyl)-pentanedioic acid (2-PMMPA) (50 mg/kg, 100 μL).²¹ All of the animals were anesthetized using 2% isoflurane during the scan.

The PET images were reconstructed using the iterative three-dimensional ordered subset expectation-maximization algorithm and the following settings: 4 iterations, 6 subsets, full detector model, low regularization, spike filter on, voxel

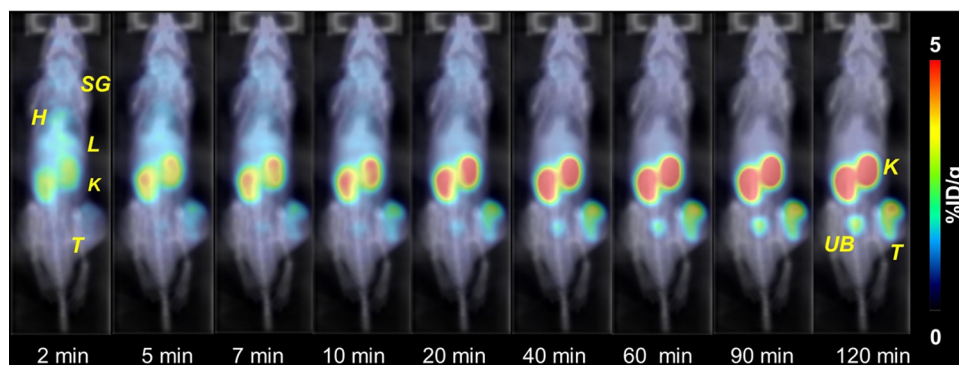


Figure 1. Serial PET/CT images of a subcutaneous prostate cancer xenograft mouse model after injection with $[^{18}\text{F}]\text{PSMA-1007}$. PET/CT, positron emission tomography/computed tomography; %ID/g, percent injected dose per gram of tissue; H, heart; K, kidney; L, liver; SG, salivary glands; T, prostate-specific membrane antigen-positive tumor (LNCaP); UB, urinary bladder.

size 0.6 mm, and 400–600 keV energy window. PET data were corrected for random, decay, scatter, and attenuation during the reconstruction. The reconstructed PET and CT images with a matrix size of $142 \times 142 \times 163 \text{ mm}^3$ and a voxel size of $0.6 \times 0.6 \times 0.6 \text{ mm}^3$ were finally prepared to be used in the analysis. PMOD software (version 3.6; PMOD Technologies, Zurich, Switzerland) was comprehensively used to process PET and CT images including activity normalization and registration.

In Vivo PET/CT Image Analysis and Quantification. Biodistribution and Pharmacokinetics. The volume of interest (VOI) was drawn manually over the major organs (tumor, salivary glands, heart, lungs, kidneys, liver, intestine, and urinary bladder) on the fused PET and CT images, taking care to ensure that the VOIs did not overlap. The number of voxels within the VOIs drawn for an organ at each time point was averaged and multiplied by the voxel volume and tissue density to estimate the organ mass. The $[^{18}\text{F}]\text{PSMA-1007}$ uptake for each organ was estimated for each mouse by applying VOIs over the respective organs on the PET images. The PET image-based biodistribution data obtained from the organs were plotted as a function of time to generate time–activity curves (TACs). For each organ, the measured activity (in kBq/cm^3) was normalized to the total injected activity to express the percentage of injected dose per gram (%ID/g). The pharmacokinetic parameters of $[^{18}\text{F}]\text{PSMA-1007}$ in each organ were evaluated quantitatively using the TACs of the organs of interest: peak concentration (C_{max}), time to reach C_{max} (T_{max}), half-life ($T_{1/2}$), and area under the TAC (AUC). The pharmacokinetic parameters were calculated using PK and PKNCA R packages.^{22,23} In estimating $T_{1/2}$, a biexponential function was used to fit the lung, heart, and liver data, and a monoexponential function was used to fit the salivary gland and intestinal data to the last three time points.

Internal Radiation Dosimetry. For this analysis, we used the data acquired from the PET/CT studies for biodistribution and pharmacokinetics. The analysis was performed in our previous report.⁵ Briefly, we applied both the organ- and voxel-level dosimetry methods. Each method is based on the Medical Internal Radiation Dose (MIRD) schema, which uses a generalized formalism for estimating the absorbed dose. S-values of the ^{18}F radioisotope for the source–target organ pairs were taken from the database published by Xie and Zaid²⁴ and the Monte Carlo approach (applied in a dedicated software called GATE ver 9.0) to simulate the complete events engaged in the radioactivity decay process, respectively. Because the

latter considers further activity distributions, organ anatomies, and tumor tissue heterogeneity on a subject-by-subject basis,^{17,25} we used it to estimate the absorbed dose in the tumor and the salivary glands that were not estimated by organ-level dosimetry due to the lack of subject-specific geometry in the MIRD-phantom.

Kinetic Analysis with an Irreversible Two-Tissue Compartment Model (2TCM) and the Image-Derived Input Function. For the subsequent repeatability and specificity analysis described below, we performed a kinetic analysis to quantify the *in vivo* tumor binding characteristics of $[^{18}\text{F}]\text{PSMA-1007}$ involving a plasma compartment (C_p), free and nonspecifically bound component in the tissue compartment (C_{NS}), and the target-specific compartment (C_s). We used an irreversible two-tissue compartment model (2T3k) with rate constants K_1 , k_2 , and k_3 ,^{7,26,27,26,27} where K_1 and k_2 are forward and reverse transport coefficients, respectively, between the C_p and C_{NS} , and k_3 represents the association of a tracer binding to the active site of the target and being internalized, i.e., C_s . In the model, the tracer was not considered to dissociate from the zinc active site of PSMA and be externalized. The time course (TAC) of $[^{18}\text{F}]\text{PSMA-1007}$ in the left ventricle (the image-derived input function, as C_p) and the tumor (as $C_{\text{NS}} + C_s$) were fitted to the model to estimate K_1 , k_2 , and k_3 . Then, the net influx rate constant was calculated as follows: $K_i = (K_1 \times k_3)/(k_2 + k_3)$.

Repeatability. Repeatability of the uptake of $[^{18}\text{F}]\text{PSMA-1007}$ was tested using datasets of separately acquired 120 min dynamic whole-body PET/CT scans, Scan 1 and Scan 2, respectively, in the same animals. The uptake of $[^{18}\text{F}]\text{PSMA-1007}$ was normalized in the standardized uptake value (SUV) rather than %ID/g to follow the unit of the diagnostic clinical convention. TAC of $[^{18}\text{F}]\text{PSMA-1007}$ in the tumor was mainly used in this analysis. Repeatability was assessed by relative difference (D), a within-subject coefficient of variation (wCV), repeatability coefficient (RC), and intraclass correlation coefficient (ICC).²⁸ The relative difference in SUV between scans was calculated as $(\text{SUV}_{\text{scan 1}} - \text{SUV}_{\text{scan 2}})/[(\text{SUV}_{\text{scan 1}} + \text{SUV}_{\text{scan 2}})/2] \times 100\%$. The wCV was calculated as the standard deviation (SD) of the relative differences over all subjects divided by $\sqrt{2}$. The RC is a threshold value within which 95% of the normal variability between measurements occurs and was calculated using symmetric limits as $1.96 \times \sqrt{2} \times \text{wCV}$. ICC was estimated using a one-way model as for each animal, two PET images were taken. The differences between

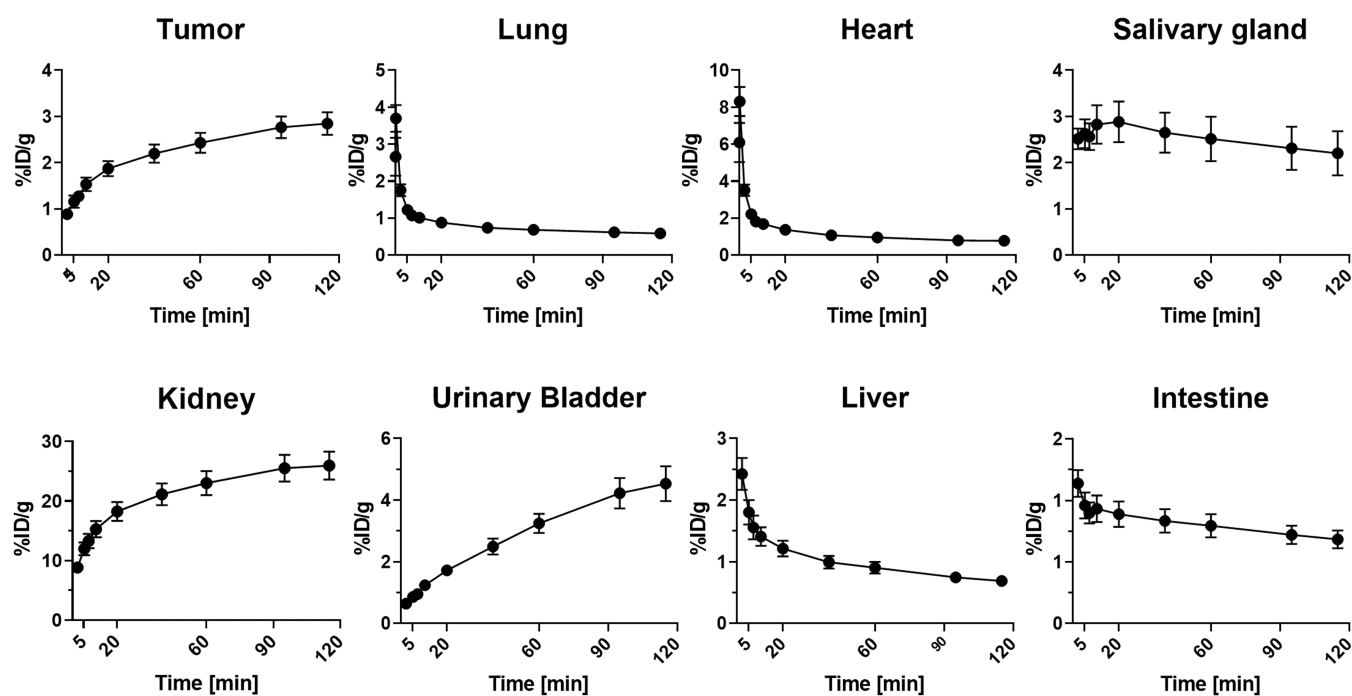


Figure 2. Percentage of injected dose per gram (%ID/g) of [^{18}F]PSMA-1007 over time. The data points represent the mean, and the error bars represent the standard error of the mean (SEM) ($n = 8$).

Table 1. Pharmacokinetic Parameters of [^{18}F]PSMA-1007^a

organ	T_{\max} (min)	C_{\max} (%ID/g)	AUC (%ID/g \times min)	$T_{1/2}$ (min)
tumor	112.5 \pm 1.64	2.86 \pm 0.24	260.98 \pm 22.99	accumulated
salivary glands	9.25 \pm 3.36	3.25 \pm 0.39	286.28 \pm 48.67	238.99 \pm 82.52
heart	0.21 \pm 0.03	8.88 \pm 0.82	132.12 \pm 9.54	0.79 \pm 0.12
lungs	0.21 \pm 0.03	3.94 \pm 0.37	88.42 \pm 7.97	0.39 \pm 0.15
kidneys	108.75 \pm 2.63	26.10 \pm 2.32	2483.88 \pm 219.37	accumulated
liver	0.38 \pm 0.05	4.18 \pm 0.47	116.15 \pm 12.30	0.44 \pm 0.21
intestine	1.13 \pm 0.25	1.47 \pm 0.14	93.35 \pm 9.98	222.73 \pm 39.93
urinary bladder	110.63 \pm 4.38	4.54 \pm 0.57	342.31 \pm 36.63	accumulated

^aAll data are presented as mean \pm SEM ($n = 8$).

scans were determined using an independent t -test with $P < 0.05$ representing statistical significance.

Specificity. The specificity of the uptake of [^{18}F]PSMA-1007 was investigated *via* group comparison analysis. The inhibition group consisted of five LNCaP tumor-bearing mice who underwent 120 min dynamic whole-body PET/CT scans preceded by PSMA-selective inhibitor 2-PMPA (50 mg/kg) treatment,²¹ and the data for the baseline group was the 120 min dynamic whole-body PET/CT images acquired for biodistribution and pharmacokinetics. The activity measured in the prostate tumor of each mouse was normalized to the total injected dose of each radiopharmaceutical and divided by the mass of the respective tumors to obtain the SUV. We plotted the SUV as a function of time to generate TACs and compared the AUCs. We also compared the rate constants (K_1 , k_2 , k_3 , and K_i) by independent t -test with a $P < 0.05$ indicating statistical significance.

RESULTS

Biodistribution and Pharmacokinetics. Figure 1 shows the biodistribution and clearance of [^{18}F]PSMA-1007 for PSMA-positive tumor (LNCaP)-bearing mice after intravenous injection. It illustrates rapid whole-body distribution

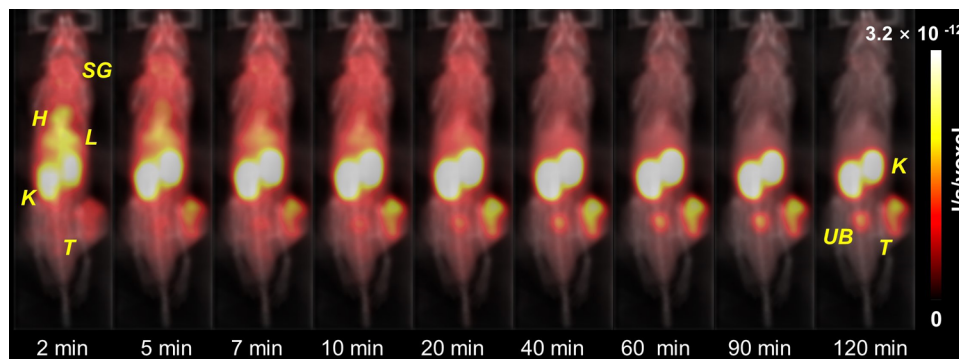
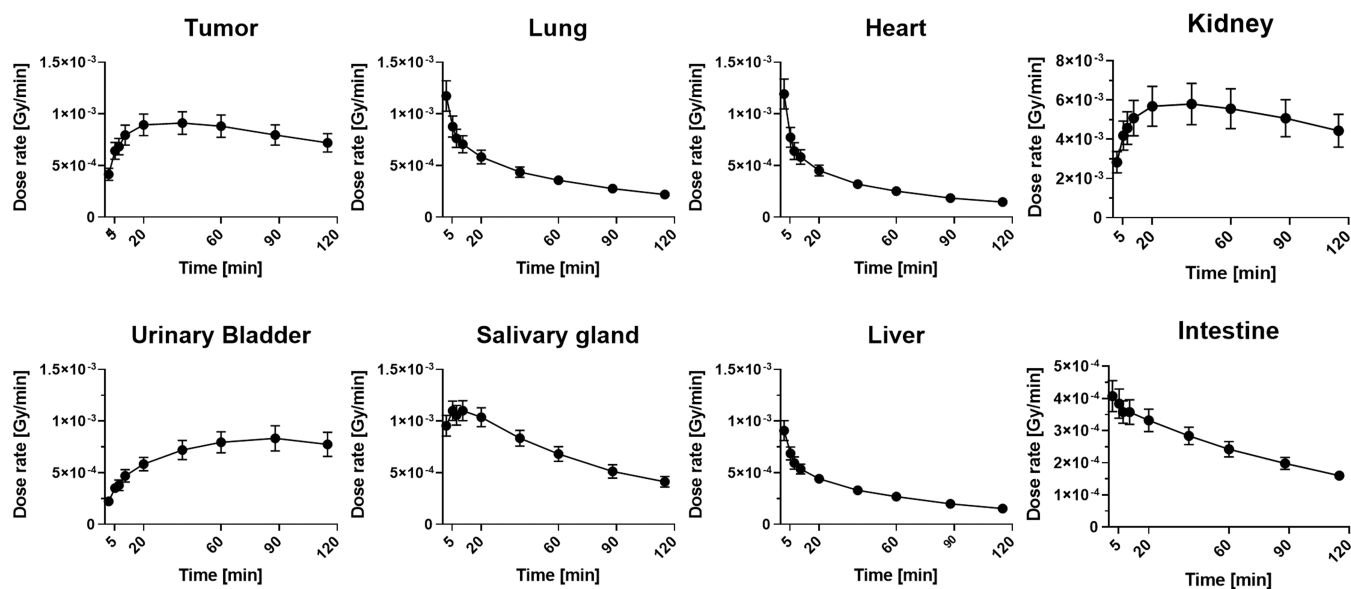
immediately after the injection, followed by rapid washout (at variable rates) from peripheral organs, including the liver, whereas other organs, namely, the kidneys, urinary bladder, and the tumor, demonstrated accumulating uptake of [^{18}F]PSMA-1007. The pharmacokinetic parameters for the visualized organs and the tumor are summarized in Figure 2 and Table 1. The kidneys showed the highest accumulation of [^{18}F]PSMA-1007 without exhibiting a washout phase during the study. The urinary bladder ($342.31 \pm 36.63\%$ ID/g \times min) was the predominant excretion route after the intravenous injection of [^{18}F]PSMA-1007 with almost 4-fold greater accumulation than that in the intestine ($93.35 \pm 9.98\%$ ID/g \times min). The tumor exhibited a peak [^{18}F]PSMA-1007 concentration of $2.86 \pm 0.24\%$ ID/g at 112 min (on average) after the injection. The off-target accumulation of [^{18}F]PSMA-1007 in the salivary glands during PSMA-targeting radiopharmaceutical therapy was substantial and exhibited a greater AUC and C_{\max} than that in the tumor.

Internal Radiation Dosimetry. The internal radiation dosimetry analysis showed that the greater the accumulation, the greater the absorbed dose. The absorbed dose estimates per organ across the method of analysis (the organ- and voxel-level dosimetry) are presented in Table 2. In both methods

Table 2. Absorbed Dose Received by Organs of the Subcutaneous Prostate Cancer Xenograft Model Mice after [¹⁸F]PSMA-1007 Administration^a

organ	voxel level (mGy/MBq)	organ level (mGy/MBq)	difference (organ level – voxel level) (mGy/MBq)
tumor	78.25 ± 10.08	NA	NA
salivary glands	35.93 ± 6.42	NA	NA
heart	10.90 ± 0.82	13.88 ± 1.12	2.98 ± 0.64
lungs	15.83 ± 1.04	12.32 ± 1.18	−3.50 ± 0.55
kidneys	441.50 ± 59.10	378.81 ± 43.97	−62.70 ± 38.75
liver	11.76 ± 0.82	4.25 ± 0.43	−7.51 ± 0.81
intestine	13.19 ± 0.76	3.66 ± 0.33	−1.84 ± 0.76
urinary bladder	54.16 ± 13.37	441.00 ± 83.18	364.35 ± 72.57

^aAll data are presented as mean ± SEM (*n* = 8). NA, not applicable.

**Figure 3.** E_{dep} maps of [¹⁸F]PSMA-1007 in tumor lesions and various organs of xenograft model mouse after injection with [¹⁸F]PSMA-1007. H, heart; K, kidney; L, liver; SG, salivary glands; T, prostate-specific membrane antigen-positive tumor (LNCaP); UB, urinary bladder.**Figure 4.** Dose rate curves of [¹⁸F]PSMA-1007 in tumor lesions and various organs of xenograft model mice. The data points represent the mean, and the error bars represent the SEM (*n* = 8).

comprehensively, the kidneys showed the highest absorbed dose (organ-level: 378.81 ± 43.97 mGy/MBq; voxel-level: 441.50 ± 59.10 mGy/MBq), whereas the highest absorbed dose was observed in the urinary bladder (441.00 ± 83.18 mGy/MBq) for the organ-level method. The absorbed dose in the other organs, excluding the kidneys, urinary bladder, salivary glands, and the tumor, ranged from 11 to 16 mGy/MBq and from 4 to 14 mGy/MBq, for voxel- and organ-level methods, respectively. Furthermore, the largest difference between the methods was observed in the urinary bladder

and kidney, possibly due to the underlying principles of estimation.

The voxel-level dosimetry method demonstrated a significant advantage in estimating the absorbed dose over the organ-level method. In the tumor and the salivary glands, the absorbed dose estimates were 78.25 ± 10.08 and 35.93 ± 6.42 mGy/MBq, respectively, whereas these values could not be estimated by organ-level dosimetry due to the lack of subject-specific tumor geometry in the MIRD-phantom. Figures 3 and

4 display the E_{dep} maps and dose rate curves over time obtained from the Monte Carlo simulations, respectively.

Repeatability. The mean TAC of [^{18}F]PSMA-1007 (SUV) in the tumor of the same animal overlapped completely between scans performed over two consecutive days. The respective fitted TACs in C_{NS} and C_{s} and corresponding parameters (K_1 – k_3 estimates and the net influx rate constant K_i) are summarized in Figure 5a and Table 3, respectively.

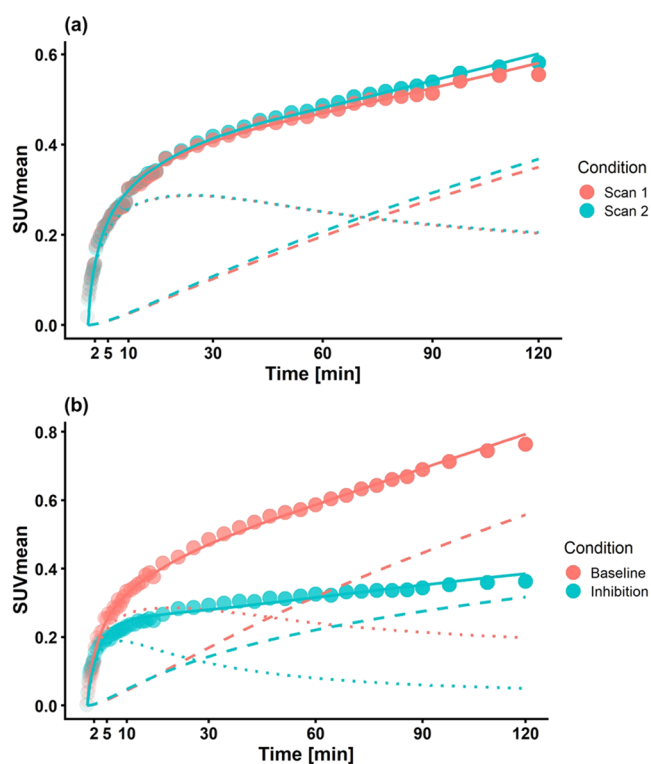


Figure 5. (a) Time–activity curves (TACs) of [^{18}F]PSMA-1007 in the irreversible two-tissue compartment model (2TCM). All tumors in the test and retest groups were evaluated ($n = 8$ in each group). (b) TACs of [^{18}F]PSMA-1007 in the irreversible 2TCM of the baseline and PSMA-inhibition groups. The data points represent the mean standard uptake value (SUV) of tumors determined by PET images. Solid lines represent the SUV estimates of a tissue compartment (C_T) using parametric parameters, dashed lines represent the SUV of a specific binding compartment (C_s), and dotted lines represent the SUV of a nonspecific binding compartment (C_{NS}).

There is no significant difference in kinetic parameters between scans ($P > 0.05$). Based on the AUC (in the unit of SUV \times min), the wCV was 7.57%, the RC was 20.98%, and the ICC

was 0.950 (95% confidence interval [CI] for ICC: 0.775, 0.99, $P < 0.001$). For SUV after 1 h, the wCV was 7.75%, the RC was 21.47%, and the ICC was 0.949 (95% CI for ICC: 0.775, 0.99, $P < 0.001$).

Specificity. Differences in SUV between the baseline and inhibition groups induced by 2-PMPA treatment (50 mg/kg) demonstrated the specific binding of [^{18}F]PSMA-1007 in the PSMA-positive tumor (LNCaP). In both the baseline and inhibition groups, the mean SUV in the tumor increased over time, with marked differences in the slope between groups; however, the TACs in the 2T3k showed a good fit in both groups. The fitted TACs for C_{NS} and C_s and the corresponding parameters of the modeling are summarized in Figure 5b and Table 3. The 2-PMPA treatment altered k_2 (efflux to the blood) and k_3 (influx to the specific binding tissue), but not K_1 (influx to the nonspecific binding tissue) and led to a 32% decrease in K_i (the net influx rate constant to the specific binding tissue) of [^{18}F]PSMA-1007 in the tumor ($P = 0.0203$).

DISCUSSION

Among the novel PSMA-targeting diagnostic radiopharmaceuticals that have recently been developed, [^{18}F]PSMA-1007 is outstanding with several advantages, including a comparatively long half-life, delayed renal excretion, and compatible structure with α -/ β -particle emitter-labeled therapeutics.^{7,12,14} PSMA-1007 shares a radiolabel-bearing moiety glutamic acids and naphthalene-based linker, which mimic the carboxylic acid groups of the DOTA chelator used in the α -/ β -particle emitter-labeled PSMA-617.¹⁶ In response to the rapid growth in the demand for clinically robust estimations of the absorbed dose–response relationship for therapeutic radiopharmaceuticals, a companion diagnostic PET is being increasingly deployed to characterize the biodistribution, pharmacokinetics, and internal radiation dosimetry of novel companion diagnostic or theranostic radiopharmaceuticals in disease/target-specific xenograft animal models. To provide a basis for clinical dose selection, dose–response relationships, and safety in terms of internal radiation dosimetry and to endorse further investigation of [^{18}F]PSMA-1007 for use in personalized medicine and TRT in cancer patients, we investigated the characteristics of [^{18}F]PSMA-1007, as well as its repeatability and specificity for target (i.e., PSMA-positive tumor) binding, in a subcutaneous prostate cancer xenograft mouse model.

Radiopharmaceuticals must satisfy several criteria to be considered for clinical cancer diagnosis, such as rapid washout from the background but high and lasting uptake in the target, thereby guaranteeing significant contrast for clear visualization and accurate quantification. The intravenously administered

Table 3. Estimated Kinetic Parameters (K_1 – k_3) and the Net Influx Rate Constant (K_i) of [^{18}F]PSMA-1007 for the Irreversible Two-Tissue Compartment Model in the Repeatability and Specificity Studies^a

study	group	K_1 (1/min)	k_2 (1/min)	k_3 (1/min)	influx- K_i (1/min)
repeatability	scan 1	0.057 \pm 0.015	0.036 \pm 0.022	0.013 \pm 0.003	0.016 \pm 0.004
	scan 2	0.057 \pm 0.016	0.033 \pm 0.015	0.014 \pm 0.005	0.017 \pm 0.005
	<i>P</i>	0.9573	0.7894	0.6439	0.7035
specificity	baseline	0.062 \pm 0.020	0.032 \pm 0.010	0.022 \pm 0.002	0.026 \pm 0.006
	inhibition	0.066 \pm 0.013	0.089 \pm 0.012	0.029 \pm 0.005	0.018 \pm 0.005
	<i>P</i>	0.7581	0.0127*	0.3514	0.0203*

^aThe twice PET/CT scans (Scan 1 and Scan 2) in the same eight mice were compared in a repeatability group. The inhibition group was treated with 2-PMPA (50 mg/kg, $n = 5$ in each group). Data were generated using an irreversible two-tissue compartment model. All data are presented as mean \pm SEM. * $P < 0.05$.

[¹⁸F]PSMA-1007 promptly exhibited whole-body distribution followed by rapid washout (at variable rates) for peripheral organs. The kidneys showed the highest accumulation of [¹⁸F]PSMA-1007 without exhibiting a washout phase during the study, as the endogenous expression of PSMA led to a substantial uptake in the kidneys.²⁹ [¹⁸F]PSMA-1007 showed high uptake in the tumor at 112 min after administration ($2.86 \pm 0.24\%ID/g$), and uptake was considerably reduced after treatment with the PSMA inhibitor 2-PMPA ($AUC_{\text{before}}: 49.66 \pm 6.72 \text{ SUV} \times \text{min}$; $AUC_{\text{after}}: 31.59 \pm 6.19 \text{ SUV} \times \text{min}$; $P = 0.0027$). Previous clinical studies have reported that the predominance of hepatobiliary excretion and delay in renal excretion benefit the detection of recurrence.^{14,30,31} [¹⁸F]PSMA-1007 has the pharmacokinetic advantage over [⁶⁸Ga]Ga-PSMA-11 of having lower uptake in the urinary bladder (SUV_{mean} in the urinary bladder, 3.66 and 25.35, respectively; $P < 0.001$).^{12,14} However, the predominant hepatobiliary excretion against the urinary bladder was only observed in human species, whereas in a preclinical environment using mice or rats, a renal dominant clearance has been described.⁷ [¹⁸F]PSMA-1007 continuously accumulated in the kidney and the urinary bladder, whereas its uptake was lower in the liver and the intestine. The difference is attributable to the biological differences between human and animal subjects in particular; the specific activity of [¹⁸F]PSMA-1007 varied unavoidably across studies. Meanwhile, the favorable pharmacokinetic characteristics in the tumor, specifically the $\sim 3\%ID/g$ peak concentration (C_{max}) 2 h after administration (T_{max}) and the longevity of the uptake in the tumor, led to the tumor exhibiting higher accumulation (AUC) than that in all organs except the kidneys and salivary glands. The uptake in the tumor at $\sim 3\%ID/g$ was found to be lower than that in the previous *in vivo* studies, which were $8.0 \pm 2.4\%ID/g$ in LNCaP tumors⁷ and $17.2 \pm 2.1\%ID/g$ in 22Rv1 tumors.³² There are many predictable reasons for a variety of tumor uptake. The partial volume effects and uncertainty in the VOI segmentation may be a reason for different *in vivo* tumor uptake regardless of PSMA expression, as described in Ioppolo et al.,³² and the qualities of experimental xenograft model mice and each tumor condition were also attributed to variability. However, in the present study, [¹⁸F]PSMA-1007 uptake in the tumors showed a significant contrast for clear visualization, accurate quantification, and specificity for diagnostic radiopharmaceutical and we confirmed our consistent VOI segmentation method through a repeatability study.

Internal radiation dosimetry analysis showed that the greater the accumulation, the greater the absorbed dose. The absorbed dose estimated by conventional organ-level dosimetry was comparatively higher than those obtained from voxel-level dosimetry, except in the organs consisting primarily of a wall and dissimilar contents, such as the heart and urinary bladder. We overcame the drawbacks of conventional dosimetry methods (the organ-level method in this study) by applying dedicated Monte Carlo simulations (the voxel-level method in this study).

Various studies have attempted to minimize the dose-limiting side effect in the off-target organs and tissues to optimize PSMA-targeted radionuclide therapy.^{33,34} Although the salivary gland is a dose-limiting organ of PSMA-targeted radionuclide therapy, it is not possible to estimate the actual absorbed dose using the MIRD schema at the organ level. As the S-values of several organs and abnormal organs in normal mice were not determined in the general MOBY mouse

phantom model, it is difficult to determine the absorbed dose in the tumor and salivary glands. A previous study addressed a similar limitation in estimating a patient's dosimetry using the sphere model of OLINDA 1.1.¹²

We estimated the absorbed dose in the tumors and salivary glands at the organ level using an alternative approach, which involved using the IDAC Spheres embedded in the IDAC-Dose 2.1 software submodule for adult reference voxel phantoms.³⁵ The absorbed dose calculated by the dosimetry software using real mouse-specific organ volume and residence time was $42.47 \pm 12.60 \text{ mGy/MBq}$ in the tumors and $212.98 \pm 44.57 \text{ mGy/MBq}$ in the salivary glands. However, this alternative method has several drawbacks. The IDAC Spheres submodule assumes that the tumor and salivary glands are a virtual uniform sphere, and the distribution of radiopharmaceuticals is homogeneous regardless of the tumor shape, location, and tissue density. Additionally, it is not applicable in mice given that mouse and human anatomical features and energy transport in these organs were determined the same and the IDAC-Dose 2.1 has been developed specifically for estimating the absorbed dose in humans. Furthermore, lower absorbed doses tend to be erroneously estimated with larger organ volumes, as the tissue density is fixed.

Using the voxel-level method, the absorbed doses in the tumors and salivary glands were estimated to be 78.25 ± 10.08 and $35.93 \pm 6.42 \text{ mGy/MBq}$, respectively. A higher absorbed dose for tumors and a lower absorbed dose for salivary glands were evaluated compared to the organ-level dosimetry-alternative approach. Meanwhile, we observed no correlation between the tumor volume and voxel-level absorbed dose, unlike the sphere model at the organ level. From this point of view, it reminds us of the value of evaluating personalized voxel-level dosimetry in various cases, such as localization, metastatic tumors, heterogeneous activity distribution, and organ geometry. Additionally, the mean absorbed dose of tumor was estimated to be 0.055 Gy/MBq higher than the previous study on [⁶⁸Ga]Ga-PSMA-11 in PSMA-positive xenograft mice which applied the same dose calculation method-GATE MC simulation ($0.024 \pm 0.003 \text{ Gy/MBq}$, $n = 3$).⁵

Although the direct Monte Carlo simulation is not time- or cost-effective, this approach addresses tissue heterogeneity and subject-specific variation in the activity distribution of real animal models using PET/CT imaging. Dose rate curves were extrapolated based on the effective half-life determined in each organ TAC and not according to the physical decay rate of ¹⁸F (half-life: 109.8 min). We estimated the absorbed dose in each organ by analytic integration of time = 0 to infinity using a more reliable time-integrated dose rate curve in the Monte Carlo simulation. This suggests that voxel-level dosimetry could yield more realistic and accurate results, particularly in abnormal organs. Our methodology for dosimetry estimation in critical organs using direct Monte Carlo simulation could be applied in clinical TRT. Furthermore, it provides a basis for the development of therapies that minimize the adverse effects associated with radiopharmaceuticals, such as xerostomia, salivary gland hypofunction, and renal toxicity.

When a therapeutic radiopharmaceutical cannot be quantitatively imaged, a surrogate imaging radiopharmaceutical can be used as a diagnostic counterpart for potential application in TRT. As the dosimetry-based activity modulation still did not play a significant role in [¹⁷⁷Lu]Lu-PSMA-617, a fixed activity of 7.4 GBq per cycle is used.^{36,37}

[¹⁸F]PSMA-1007, with a similar motif to that of PSMA-617, shows similar biodistribution and pharmacokinetics and is used in tandem with [¹⁷⁷Lu]Lu-PSMA-617.¹⁶ Due to its unique chemical structure and biological characteristics, [¹⁸F]PSMA-1007 can be used to investigate the injected dose of radiolabeled PSMA-617 to optimize treatment prior to a new therapy cycle and decrease uptake in nontarget organs.⁷

In terms of theranostic dosimetry, an immediate challenge is the validation of the extrapolation between two radionuclides with different physical half-lives. For example, the half-life of ²²⁵Ac is 10 days, that of ¹⁷⁷Lu is 8.02 days, and for its theranostic counterpart, ¹⁸F, it is 109.8 min. Few reports have compared diagnostic and therapeutic radiopharmaceuticals; instead, it is assumed that theranostic pairs have similar biodistribution and pharmacokinetics.^{38–40} The radioactivity of therapeutic radiopharmaceuticals is estimated by the difference in the physical half-life between two nuclides. The radioactivity of therapeutic radiopharmaceuticals can be calculated by the physical half-life of each radionuclide with a biological half-life of [¹⁸F]PSMA-1007 using the formula

$$A_T(t) = A_I(t)e^{t \ln 2 / T_{1/2,I}} e^{-t \ln 2 / T_{1/2,T}}$$

where $A_T(t)$ is the activity of therapeutic radiopharmaceuticals in time t and $A_I(t)$ is the activity of imaging radiopharmaceuticals in time t . It is necessary to investigate whether the extrapolated TAC from imaging radiopharmaceutical is equal to the real data on therapeutic radiopharmaceutical. So further research for investigating determining acquisition time to capture accumulation in the tissue of interest using shorter physical half-life imaging radiopharmaceutical and the fitting method to extrapolate the rest of the curve is required. If this assumption is validated by additional research, we could use a positron-emitting surrogate imaging radiopharmaceutical sharing a similar motif of therapeutics applied with extrapolating methods (from [¹⁸F]PSMA-1007 to [¹⁷⁷Lu]Lu-/[²²⁵Ac]Ac-PSMA-617 in this study). As a result, dose distribution in prostate cancer and critical organs is more reliable rather than a non/less-quantitative molecular image.

We estimated the human residence time of [¹⁸F]PSMA-1007 from our xenograft model mice proposed by Constantinescu et al.⁴¹ The organ and whole-body weight difference between species^{42,43} was used for normalization and IDAC–Dose 2.1 software calculated the human effective dose. The effective dose of $1.12 \times 10^{-2} \pm 1.39 \times 10^{-4}$ mSv/MBq was predicted based on ICRP adult reference voxel phantoms³⁵ and was less than that predicted by a previous clinical study.¹² Further research is required to investigate more reliable new methods than organ/whole-body weight normalization for translating human absorbed dose from the preclinical study and gather sufficient evidence about determining the human effective dose of [¹⁷⁷Lu]Lu-PSMA-617 directly from preclinical xenograft model mice after administering [¹⁸F]PSMA-1007.

The development of a quantitative imaging biomarker requires an understanding of the biomarker's technical performance, including estimates of measurement linearity, bias, error, repeatability, and reproducibility. We determined good repeatability for the tumor uptake of [¹⁸F]PSMA-1007 in xenograft mice between the scans from dynamic PET imaging, wCVs, RCs, and ICCs results obtained over two consecutive days. Our findings are comparable to those of previous studies

on [⁶⁸Ga]Ga-PSMA-11 and [⁶⁸Ga]Ga-DP11 in PSMA-positive xenograft mice.^{44,45}

Furthermore, we found that the inhibition of PSMA by 2-PMPA reduced the AUC of the TAC over 120 min by 37%. The 2-PMPA treatment altered k_2 and k_3 , but not K_1 ; the net influx rate constant K_i and concentration in specific binding tissue (C_S) were also reduced in the inhibition group. Conclusively, the uptake of [¹⁸F]PSMA-1007 could be blocked by a sufficient amount of 2-PMPA, indicating the high specificity of the radiopharmaceutical.

One limitation of our study is that the scan duration time does not allow for a representative evaluation of [¹⁸F]PSMA-1007 excretion in mice and full excretion from several organs. We determined the imaging scan time for this study by considering previously published preclinical and clinical studies. In 2016, preclinical PET imaging acquisition was performed for 3600 s in the list mode and a second scan was carried out 2 h after [¹⁸F]PSMA-1007 injection.⁷ Several clinical studies have settled on imaging at 2 h post-injection^{13,46,47} and earlier imaging times between 45 and 120 min have also been reported.^{14,31,48,49} Although dynamic 2 h is only a 1-fold half-life of ¹⁸F, our imaging protocol was enough to estimate the absorbed dose by calculating the AUC of dose rate curves after the Monte Carlo simulation.

Over 120 min of PET imaging showed the accumulation of [¹⁸F]PSMA-1007 in the tumor, urinary bladder, and kidneys. We suggest that accumulation in these organs resulted in lower rates of hepatobiliary excretion compared to those found by previous clinical studies^{26,50} and overestimation of residence time when applying the MIRD schema. However, the E_{dep} maps and dose maps were produced using subject-specific PET/CT images as input data, and a subject-/organ-specific dose rate curve was produced. Owing to the more reliable estimation of the absorbed dose at the voxel level, we addressed the overestimation at the organ level and the small sample size inherent in the short scan duration.

In this study, we attempted to demonstrate a preclinical research paradigm to advance the use of voxel-level dosimetry in TRT to deliver personalized dosimetry considering patient-specific heterogeneous tissue compositions and activity distributions. Although [¹⁸F]PSMA-1007 has been investigated in several clinical and preclinical studies for evaluating diagnostic efficacy, preclinical voxel-level dosimetry has not been yet performed with regard to personalization and precision medicine. Particularly, during multiple cycle therapy, such as with [¹⁷⁷Lu]Lu-PSMA-617, voxel-level dosimetry-guided response assessment is essential not only for formulating the therapy plans but also post treatment. Preclinical voxel-level dosimetry of [¹⁸F]PSMA-1007 can be used as the fundamental basis for describing the surrogacy for [¹⁷⁷Lu]Lu-/[²²⁵Ac]Ac-PSMA-617 and developing the curve fitting method for a more accurate time–activity curve and dosimetry estimates.

CONCLUSIONS

In this study, we proved the value of preclinical evaluation for determining the clinical usefulness of [¹⁸F]PSMA-1007 in a disease mouse model. By assessing its biodistribution and pharmacokinetics in xenograft mice, we determined that [¹⁸F]PSMA-1007 was an effective diagnostic radiopharmaceutical for the detection of prostate cancers with high specificity. Dosimetry at the voxel level was used to accurately determine the absorbed dose not only in major organs but also in

abnormal tumors and dose-limiting critical organs, such as the salivary glands and kidneys. We believe that our preclinical study of internal radiation dosimetry at the organ and voxel levels using [^{18}F]PSMA-1007 in xenograft mice showed great promise for use in patient-specific dosimetry and that [^{18}F]PSMA-1007 could potentially serve as a surrogate imaging radiopharmaceutical during prostate-targeted radionuclide therapy. The approach of voxel-based dosimetry of companion diagnostics proposed in the present study could be used for assessing the three-dimensional distribution of the absorbed dose for α - and/or β -particle emitter-labeled therapeutics, for which estimating the radiation doses quantitatively is difficult via imaging. For example, ^{225}Ac -DOTATATE coupled with ^{68}Ga -DOTANOC in targeted α therapy of neuroendocrine tumors, $^{51,225}\text{Ac}$ -labeled hNd2 (NMT25) coupled with ^{89}Zr -labeled hNd2 (NMK89) for therapy of pancreatic cancer, 52 and ^{225}Ac -DOTA-hTAB004 coupled with ^{111}In -DOTA-hTAB004 for therapy of breast cancer. 53

AUTHOR INFORMATION

Corresponding Authors

Hyun Soo Park – Department of Nuclear Medicine, Seoul National University College of Medicine, Seoul National University Bundang Hospital, Seongnam 13620, Korea; Department of Molecular Medicine and Biopharmaceutical Sciences, Graduate School of Convergence Science and Technology, Seoul National University, Seoul 08826, Korea; Phone: +82-31-787-2936; Email: hyuns@snu.ac.kr; Fax: +82-31-787-4018

Mijin Yun – Department of Nuclear Medicine, Severance Hospital, Yonsei University College of Medicine, Seoul 03722, Korea; Phone: +82-2-2228-6068; Email: yunmijin@yuhs.ac; Fax: +82-2-2227-8354

Sang Eun Kim – Department of Nuclear Medicine, Seoul National University College of Medicine, Seoul National University Bundang Hospital, Seongnam 13620, Korea; Department of Molecular Medicine and Biopharmaceutical Sciences, Graduate School of Convergence Science and Technology, Seoul National University, Seoul 08826, Korea; Advanced Institutes of Convergence Technology, Suwon 16229, Korea; BIK Therapeutics Inc., Bundang-gu, Seongnam 13605, Korea; Phone: +82-31-787-7671; Email: kse@snu.ac.kr; Fax: +82-31-787-4018

Authors

Su Bin Kim – Department of Applied Bioengineering, Graduate School of Convergence Science and Technology, Seoul National University, Seoul 08826, Korea; Department of Nuclear Medicine, Seoul National University College of Medicine, Seoul National University Bundang Hospital, Seongnam 13620, Korea; orcid.org/0000-0002-9948-2905

In Ho Song – Department of Nuclear Medicine, Seoul National University College of Medicine, Seoul National University Bundang Hospital, Seongnam 13620, Korea

Seon Yoo Kim – Department of Nuclear Medicine, Severance Hospital, Yonsei University College of Medicine, Seoul 03722, Korea

Hae Young Ko – Department of Nuclear Medicine, Severance Hospital, Yonsei University College of Medicine, Seoul 03722, Korea

Hee Seup Kil – Research Institute of Radiopharmaceuticals, FutureChem Co. Ltd, Seoul 04793, Korea

Dae Yoon Chi – Research Institute of Radiopharmaceuticals, FutureChem Co. Ltd, Seoul 04793, Korea

Frederik L. Giesel – Department of Nuclear Medicine, Heinrich-Heine-University, University Hospital Duesseldorf, Duesseldorf 40225, Germany

Klaus Kopka – Institute of Radiopharmaceutical Cancer Research, Helmholtz-Zentrum Dresden-Rossendorf (HZDR) e.v., Dresden 01328, Germany; Technische Universität Dresden, Faculty of Chemistry and Food Chemistry, School of Science, Dresden 01069, Germany; National Center for Tumor Diseases (NCT) Dresden, University Hospital Carl Gustav Carus, Dresden 01307, Germany; German Cancer Consortium (DKTK), Partner Site Dresden, Dresden 01307, Germany

Alexander Hoepping – Department of Medicinal Chemistry, ABX Advanced Biochemical Compounds GmbH, Radeberg 1454, Germany

Joong-Hyun Chun – Department of Nuclear Medicine, Severance Hospital, Yonsei University College of Medicine, Seoul 03722, Korea; orcid.org/0000-0002-9665-7829

Complete contact information is available at:

<https://pubs.acs.org/10.1021/acs.molpharmaceut.2c00788>

Author Contributions

S.B.K., I.H.S., S.Y.K., H.Y.K., H.S.P., and M.J.Y. conceived and planned the experiments. S.B.K., I.H.S., and H.S.P. performed the experiments. S.B.K. and H.S.P. planned and performed the interpretation of imaging data and simulations. F.L.G., K.K., and A.H. performed the synthesis of precursors. H.S.K., D.Y.C., and J.H.C. carried out the radiosynthesis of [^{18}F]PSMA-1007. S.B.K., S.Y.K., H.Y.K., I.H.S., H.S.P., M.J.Y., and S.E.K. interpreted the results. As the first author, SBK mainly wrote the manuscript, and all authors contributed to its revision. All authors have given approval to the final version of the manuscript.

Funding

This research was supported by the SNUBH (Seoul National University Bundang Hospital) Research Fund (14-2021-0005), Seoul National University Research Grant in 2020, BK21FOUR Program of the National Research Foundation of Korea (NRF) funded by the Ministry of Education (S120200513755), Basic Science Research Program through the National Research Foundation of Korea (NRF) funded by the Ministry of Science and ICT (No. NRF-2016K1A3A1A48954034). This work was partly funded by a grant of the Federal Ministry of Education and Research (BMBF), project ProstaPET (2U2WTZKOREA-021; no. 01DR17031A).

Notes

The authors declare the following competing financial interest(s): Frederik L. Giesel is the coinventor of PSMA-1007 and an advisor in ABX Radeberg, Telix Pharmaceuticals, and SOFIE Biosciences. Klaus Kopka is the coinventor of PSMA-1007 and a member of the SAB of Telix Pharmaceuticals.

ABBREVIATIONS

%ID/g, percentage of injected dose per organ tissue; 2TCM, two-tissue compartment model; AUC, area under the curve; CT, computed tomography; D, relative difference; GATE,

Geant4 application for tomographic emission; HPLC, high-performance liquid chromatography; ICC, intraclass correlation coefficient; LNCaP, lymph node carcinoma of the prostate; MIRD, medical internal radiation dose; PET, positron emission tomography; PSMA, prostate-specific membrane antigen; QC, quality control; QMA, quaternary methyl ammonium; RC, repeatability coefficient; RCY, radiochemical yield; SD, standard deviation; SEM, standard error of the mean; SPE, solid-phase extraction; SUV, standard uptake value; TAC, time–activity curve; TBAF, tetrabutylammonium fluoride; TFA, trifluoroacetic acid; TLC, thin-layer chromatography; VOI, volume of interest; wCV, within-subject coefficient of variation; WFI, water for injection

REFERENCES

- (1) Zippel, C.; Ronski, S. C.; Bohnet-Joschko, S.; Giesel, F. L.; Kopka, K. Current Status of PSMA-Radiotracers for Prostate Cancer: Data Analysis of Prospective Trials Listed on ClinicalTrials.gov. *Pharmaceuticals* **2020**, *13*, No. 12.
- (2) Eder, M.; Schäfer, M.; Bauder-Wüst, U.; Hull, W.-E.; Wängler, C.; Mier, W.; Haberkorn, U.; Eisenhut, M. 68Ga-Complex Lipophilicity and the Targeting Property of a Urea-Based PSMA Inhibitor for PET Imaging. *Bioconjugate Chem.* **2012**, *23*, 688–697.
- (3) Afshar-Oromieh, A.; Avtzi, E.; Giesel, F. L.; Holland-Letz, T.; Linhart, H. G.; Eder, M.; Eisenhut, M.; Boxler, S.; Hadaschik, B. A.; Kratochwil, C.; Weichert, W.; Kopka, K.; Debus, J.; Haberkorn, U. The Diagnostic Value of PET/CT Imaging with the (68)Ga-Labelled PSMA Ligand HBED-CC in the Diagnosis of Recurrent Prostate Cancer. *Eur. J. Nucl. Med. Mol. Imaging* **2015**, *42*, 197–209.
- (4) Afshar-Oromieh, A.; Holland-Letz, T.; Giesel, F. L.; Kratochwil, C.; Mier, W.; Haufe, S.; Debus, N.; Eder, M.; Eisenhut, M.; Schäfer, M.; Neels, O.; Hohenfellner, M.; Kopka, K.; Kauczor, H.-U.; Debus, J.; Haberkorn, U. Diagnostic Performance of 68Ga-PSMA-11 (HBED-CC) PET/CT in Patients with Recurrent Prostate Cancer: Evaluation in 1007 Patients. *Eur. J. Nucl. Med. Mol. Imaging* **2017**, *44*, 1258–1268.
- (5) Kim, S. B.; Song, I. H.; Song, Y. S.; Lee, B. C.; Gupta, A.; Lee, J. S.; Park, H. S.; Kim, S. E. Biodistribution and Internal Radiation Dosimetry of a Companion Diagnostic Radiopharmaceutical, [68Ga]-PSMA-11, in Subcutaneous Prostate Cancer Xenograft Model Mice. *Sci. Rep.* **2021**, *11*, No. 15263.
- (6) Schwarzenboeck, S. M.; Rauscher, I.; Bluemel, C.; Fendler, W. P.; Rowe, S. P.; Pomper, M. G.; Afshar-Oromieh, A.; Herrmann, K.; Eiber, M. PSMA Ligands for PET Imaging of Prostate Cancer. *J. Nucl. Med.* **2017**, *58*, 1545–1552.
- (7) Cardinale, J.; Schäfer, M.; Benešová, M.; Bauder-Wüst, U.; Leotta, K.; Eder, M.; Neels, O. C.; Haberkorn, U.; Giesel, F. L.; Kopka, K. Preclinical Evaluation of 18F-PSMA-1007, a New Prostate-Specific Membrane Antigen Ligand for Prostate Cancer Imaging. *J. Nucl. Med.* **2017**, *58*, 425–431.
- (8) Shamni, O.; Nebeling, B.; Grievink, H.; Mishani, E. Fine-Tuning of the Automated [18 F]PSMA-1007 Radiosynthesis. *J. Labelled Compd. Radiopharm.* **2019**, *62*, 252–258.
- (9) Maisto, C.; Morisco, A.; de Marino, R.; Squame, E.; Porfidia, V.; D'Ambrosio, L.; Di Martino, D.; Gaballo, P.; Aurilio, M.; Buonanno, M.; Esposito, A.; Raddi, M.; Lastoria, S. On Site Production of [18F]PSMA-1007 Using Different [18F]Fluoride Activities: Practical, Technical and Economical Impact. *EJNMMI Radiopharm. Chem.* **2021**, *6*, 36.
- (10) Sanchez-Crespo, A. Comparison of Gallium-68 and Fluorine-18 Imaging Characteristics in Positron Emission Tomography. *Appl. Radiat. Isot.* **2013**, *76*, 55–62.
- (11) Hong, J.-J.; Liu, B.; Wang, Z.-Q.; Tang, K.; Ji, X.-W.; Yin, W.-W.; Lin, J.; Zheng, X.-W. The Value of 18F-PSMA-1007 PET/CT in Identifying Non-Metastatic High-Risk Prostate Cancer. *EJNMMI Res.* **2020**, *10*, 138.
- (12) Giesel, F. L.; Hadaschik, B.; Cardinale, J.; Radtke, J.; Vinsensia, M.; Lehnert, W.; Kesch, C.; Tolstov, Y.; Singer, S.; Grabe, N.; Duensing, S.; Schäfer, M.; Neels, O. C.; Mier, W.; Haberkorn, U.; Kopka, K.; Kratochwil, C. F-18 Labelled PSMA-1007: Biodistribution, Radiation Dosimetry and Histopathological Validation of Tumor Lesions in Prostate Cancer Patients. *Eur. J. Nucl. Med. Mol. Imaging* **2017**, *44*, 678–688.
- (13) Giesel, F. L.; Will, L.; Lawal, I.; Lengana, T.; Kratochwil, C.; Vorster, M.; Neels, O.; Reyneke, F.; Haberkorn, U.; Kopka, K.; Sathegke, M. Intraindividual Comparison of 18F-PSMA-1007 and 18F-DCFPyL PET/CT in the Prospective Evaluation of Patients with Newly Diagnosed Prostate Carcinoma: A Pilot Study. *J. Nucl. Med.* **2018**, *59*, 1076–1080.
- (14) Kuten, J.; Fahoum, I.; Savin, Z.; Shamni, O.; Gitstein, G.; Hershkovitz, D.; Mabjeesh, N. J.; Yossepowitch, O.; Mishani, E.; Even-Sapir, E. Head-to-Head Comparison of 68Ga-PSMA-11 with 18F-PSMA-1007 PET/CT in Staging Prostate Cancer Using Histopathology and Immunohistochemical Analysis as a Reference Standard. *J. Nucl. Med.* **2020**, *61*, 527–532.
- (15) Sprute, K.; Kramer, V.; Koerber, S. A.; Meneses, M.; Fernandez, R.; Soza-Ried, C.; Eiber, M.; Weber, W. A.; Rauscher, I.; Rahbar, K.; Schaefer, M.; Watabe, T.; Uemura, M.; Naka, S.; Nonomura, N.; Hatazawa, J.; Schwab, C.; Schütz, V.; Hohenfellner, M.; Holland-Letz, T.; Giesel, F. L.; et al. Diagnostic Accuracy of 18F-PSMA-1007 PET/CT Imaging for Lymph Node Staging of Prostate Carcinoma in Primary and Biochemical Recurrence. *J. Nucl. Med.* **2021**, *62*, 208–213.
- (16) Giesel, F. L.; Cardinale, J.; Schäfer, M.; Neels, O.; Benešová, M.; Mier, W.; Haberkorn, U.; Kopka, K.; Kratochwil, C. (18)F-Labelled PSMA-1007 Shows Similarity in Structure, Biodistribution and Tumour Uptake to the Theragnostic Compound PSMA-617. *Eur. J. Nucl. Med. Mol. Imaging* **2016**, *43*, 1929–1930.
- (17) Gupta, A.; Lee, M. S.; Kim, J. H.; Park, S.; Park, H. S.; Kim, S. E.; Lee, D. S.; Lee, J. S. Preclinical Voxel-Based Dosimetry through GATE Monte Carlo Simulation Using PET/CT Imaging of Mice. *Phys. Med. Biol.* **2019**, *64*, No. 095007.
- (18) Gupta, A.; Shin, J. H.; Lee, M. S.; Park, J. Y.; Kim, K.; Kim, J. H.; Suh, M.; Park, C. R.; Kim, Y. J.; Song, M. G.; Jeong, J. M.; Lee, D. S.; Lee, Y.-S.; Lee, J. S. Voxel-Based Dosimetry of Iron Oxide Nanoparticle-Conjugated 177Lu-Labeled Folic Acid Using SPECT/CT Imaging of Mice. *Mol. Pharmaceutics* **2019**, *16*, 1498–1506.
- (19) Cardinale, J.; Martin, R.; Remde, Y.; Schäfer, M.; Hienzsch, A.; Hübner, S.; Zerges, A.-M.; Marx, H.; Hesse, R.; Weber, K.; Smits, R.; Hoepfing, A.; Müller, M.; Neels, O. C.; Kopka, K. Procedures for the GMP-Compliant Production and Quality Control of [18F]PSMA-1007: A Next Generation Radiofluorinated Tracer for the Detection of Prostate Cancer. *Pharmaceuticals* **2017**, *10*, No. 77.
- (20) European Pharmacopoeia (Ph. Eur.) 10th Edition—European Directorate for the Quality of Medicines & HealthCare. <https://www.edqm.eu/en/web/edqm/european-pharmacopoeia-ph-eur-10th-edition> (accessed Aug 7, 2022).
- (21) Hillier, S. M.; Maresca, K. P.; Femia, F. J.; Marquis, J. C.; Foss, C. A.; Nguyen, N.; Zimmerman, C. N.; Barrett, J. A.; Eckelman, W. C.; Pomper, M. G.; Joyal, J. L.; Babich, J. W. Preclinical Evaluation of Novel Glutamate-Urea-Lysine Analogues That Target Prostate-Specific Membrane Antigen as Molecular Imaging Pharmaceuticals for Prostate Cancer. *Cancer Res.* **2009**, *69*, 6932–6940.
- (22) Jaki, T.; Wolfsegger, M. J. Estimation of Pharmacokinetic Parameters with the R Package PK. *Pharm. Stat.* **2011**, *10*, 284–288.
- (23) Buckeridge, C.; Duvvuri, S.; Denney, W. S. Simple, Automatic Noncompartmental Analysis: The PKNCA R Package. *J. Pharmacokinetics. Pharmacodyn.* **2015**, *42*, 11–107.
- (24) Xie, T.; Zaidi, H. Monte Carlo-Based Evaluation of S-Values in Mouse Models for Positron-Emitting Radionuclides. *Phys. Med. Biol.* **2013**, *58*, 169–182.
- (25) Lee, M. S.; Kim, J. H.; Paeng, J. C.; Kang, K. W.; Jeong, J. M.; Lee, D. S.; Lee, J. S. Whole-Body Voxel-Based Personalized Dosimetry: The Multiple Voxel S-Value Approach for Heterogeneous

Media with Nonuniform Activity Distributions. *J. Nucl. Med.* **2018**, *59*, 1133–1139.

(26) Sachpekidis, C.; Afshar-Oromieh, A.; Kopka, K.; Strauss, D. S.; Pan, L.; Haberkorn, U.; Dimitrakopoulou-Strauss, A. 18F-PSMA-1007 Multiparametric, Dynamic PET/CT in Biochemical Relapse and Progression of Prostate Cancer. *Eur. J. Nucl. Med. Mol. Imaging* **2020**, *47*, 592–602.

(27) McDermott, S.; Yan, D. WE-C-217BCD-12: Irreversible Two-Tissue Compartment Model Fitting for Dynamic 18F-FDG PET: A Practical Comparison of Methods Using Simulated Time-Activity Data. *Med. Phys.* **2012**, *39*, 3952.

(28) Baumgartner, R.; Joshi, A.; Feng, D.; Zanderigo, F.; Ogden, R. T. Statistical Evaluation of Test-Retest Studies in PET Brain Imaging. *EJNMMI Res.* **2018**, *8*, 13.

(29) Bacich, D. J.; Pinto, J. T.; Tong, W. P.; Heston, W. D. Cloning, Expression, Genomic Localization, and Enzymatic Activities of the Mouse Homolog of Prostate-Specific Membrane Antigen/NAALADase/Folate Hydrolase. *Mamm. Genome* **2001**, *12*, 117–123.

(30) Giesel, F. L.; Will, L.; Kesch, C.; Freitag, M.; Kremer, C.; Merkle, J.; Neels, O. C.; Cardinale, J.; Hadaschik, B.; Hohenfellner, M.; Kopka, K.; Haberkorn, U.; Kratochwil, C. Biochemical Recurrence of Prostate Cancer: Initial Results with [18F]PSMA-1007 PET/CT. *J. Nucl. Med.* **2018**, *59*, 632–635.

(31) Giesel, F. L.; Knorr, K.; Spohn, F.; Will, L.; Maurer, T.; Flechsig, P.; Neels, O.; Schiller, K.; Amaral, H.; Weber, W. A.; Haberkorn, U.; Schwaiger, M.; Kratochwil, C.; Choyke, P.; Kramer, V.; Kopka, K.; Eiber, M. Detection Efficacy of 18F-PSMA-1007 PET/CT in 251 Patients with Biochemical Recurrence of Prostate Cancer After Radical Prostatectomy. *J. Nucl. Med.* **2019**, *60*, 362–368.

(32) Ioppolo, J. A.; Nezhich, R. A.; Richardson, K. L.; Morandau, L.; Leedman, P. J.; Price, R. I. Direct in Vivo Comparison of [18F]PSMA-1007 with [68Ga]Ga-PSMA-11 and [18F]AlF-PSMA-11 in Mice Bearing PSMA-Expressing Xenografts. *Appl. Radiat. Isot.* **2020**, *161*, No. 109164.

(33) Soeda, F.; Watabe, T.; Naka, S.; Liu, Y.; Horitsugi, G.; Neels, O. C.; Kopka, K.; Tatsumi, M.; Shimosegawa, E.; Giesel, F. L.; Hatazawa, J. Impact of 18F-PSMA-1007 Uptake in Prostate Cancer Using Different Peptide Concentrations: Preclinical PET/CT Study on Mice. *J. Nucl. Med.* **2019**, *60*, 1594–1599.

(34) Heynickx, N.; Herrmann, K.; Vermeulen, K.; Baatout, S.; Aerts, A. The Salivary Glands as a Dose Limiting Organ of PSMA-Targeted Radionuclide Therapy: A Review of the Lessons Learnt so Far. *Nucl. Med. Biol.* **2021**, *98–99*, 30–39.

(35) Andersson, M.; Johansson, L.; Eckerman, K.; Mattsson, S. IDAC-Dose 2.1, an Internal Dosimetry Program for Diagnostic Nuclear Medicine Based on the ICRP Adult Reference Voxel Phantoms. *EJNMMI Res.* **2017**, *7*, 88.

(36) US Food and Drug Administration. Center for Drug Evaluation and Research, Labeling: Application Number: 208700Orig1s000. Last Revised January 2018, 2022. https://www.accessdata.fda.gov/drugsatfda_docs/nda/2018/208700Orig1s000lbl.pdf (accessed Jun 19, 2022).

(37) Hromadik, L. K.; Sturges, L. Caring for Patients Receiving 177Lu-DOTATATE, Lutathera: A Treatment of Hope for Patients With Gastroenteropancreatic Neuroendocrine Tumors. *J. Radiol. Nurs.* **2019**, *38*, 28–32.

(38) Rösch, F.; Herzog, H.; Qaim, S. M. The Beginning and Development of the Theranostic Approach in Nuclear Medicine, as Exemplified by the Radionuclide Pair 86Y and 90Y. *Pharmaceutics* **2017**, *10*, 10.

(39) Förster, G. J.; Engelbach, M. J.; Brockmann, J. J.; Reber, H. J.; Buchholz, H. G.; Mäcke, H. R.; Rösch, F. R.; Herzog, H. R.; Bartenstein, P. R. Preliminary Data on Biodistribution and Dosimetry for Therapy Planning of Somatostatin Receptor Positive Tumours: Comparison of (86)Y-DOTATOC and (111)In-DTPA-Octreotide. *Eur. J. Nucl. Med.* **2001**, *28*, 1743–1750.

(40) Dalm, S. U.; Bakker, I. L.; de Blois, E.; Doeswijk, G. N.; Konijnenberg, M. W.; Orlandi, F.; Barbato, D.; Tedesco, M.; Maina, T.; Nock, B. A.; de Jong, M. 68Ga/177Lu-NeoBOMB1, a Novel

Radiolabeled GRPR Antagonist for Theranostic Use in Oncology. *J. Nucl. Med.* **2017**, *58*, 293–299.

(41) Constantinescu, C. C.; Sevrioukov, E.; Garcia, A.; Pan, M.-L.; Mukherjee, J. Evaluation of [18F]Mefway Biodistribution and Dosimetry Based on Whole-Body PET Imaging of Mice. *Mol. Imaging Biol.* **2013**, *15*, 222–229.

(42) Cristy, M.; Eckerman, K. F. *Specific Absorbed Fractions of Energy at Various Ages from Internal Photon Sources: 7, Adult Male*; Oak Ridge National Laboratory (ORNL): Oak Ridge, TN, United States, 1987.

(43) Keenan, M. A.; Stabin, M. G.; Segars, W. P.; Fernald, M. J. RADAR Realistic Animal Model Series for Dose Assessment. *J. Nucl. Med.* **2010**, *51*, 471–476.

(44) Osborne, J. R.; Kalidindi, T. M.; Punzalan, B. J.; Gangangari, K.; Spratt, D. E.; Weber, W. A.; Larson, S. M.; Pillarsetty, N. V. K. Repeatability of [68Ga]DKFZ11-PSMA PET Scans for Detecting Prostate-Specific Membrane Antigen-Positive Prostate Cancer. *Mol. Imaging Biol.* **2017**, *19*, 944–951.

(45) Lücknerath, K.; Stuparu, A. D.; Wei, L.; Kim, W.; Radu, C. G.; Mona, C. E.; Calais, J.; Rettig, M.; Reiter, R. E.; Czernin, J.; Slavik, R.; Herrmann, K.; Eiber, M.; Fendler, W. P. Detection Threshold and Reproducibility of 68Ga-PSMA11 PET/CT in a Mouse Model of Prostate Cancer. *J. Nucl. Med.* **2018**, *59*, 1392–1397.

(46) Dietlein, F.; Kobe, C.; Hohberg, M.; Zlatopolskiy, B. D.; Krapf, P.; Endepols, H.; Täger, P.; Hammes, J.; Heidenreich, A.; Persigehl, T.; Neumaier, B.; Drzezga, A.; Dietlein, M. Intraindividual Comparison of 18F-PSMA-1007 with Renally Excreted PSMA Ligands for PSMA PET Imaging in Patients with Relapsed Prostate Cancer. *J. Nucl. Med.* **2020**, *61*, 729–734.

(47) Rahbar, K.; Afshar-Oromieh, A.; Seifert, R.; Wagner, S.; Schäfers, M.; Bögemann, M.; Weckesser, M. Diagnostic Performance of 18F-PSMA-1007 PET/CT in Patients with Biochemical Recurrent Prostate Cancer. *Eur. J. Nucl. Med. Mol. Imaging* **2018**, *45*, 2055–2061.

(48) Witkowska-Patena, E.; Giżewska, A.; Dziuk, M.; Miśko, J.; Budzyńska, A.; Wałęcka-Mazur, A. Head-to-Head Comparison of 18F-Prostate-Specific Membrane Antigen-1007 and 18F-Fluorocholeline PET/CT in Biochemically Relapsed Prostate Cancer. *Clin. Nucl. Med.* **2019**, *44*, e629–e633.

(49) Foley, R. W.; Redman, S. L.; Graham, R. N.; Loughborough, W. W.; Little, D. Fluorine-18 Labeled Prostate-Specific Membrane Antigen (PSMA)-1007 Positron-Emission Tomography-Computed Tomography: Normal Patterns, Pearls, and Pitfalls. *Clin. Radiol.* **2020**, *75*, 903–913.

(50) Rahbar, K.; Afshar-Oromieh, A.; Bögemann, M.; Wagner, S.; Schäfers, M.; Stegger, L.; Weckesser, M. 18F-PSMA-1007 PET/CT at 60 and 120 Minutes in Patients with Prostate Cancer: Biodistribution, Tumour Detection and Activity Kinetics. *Eur. J. Nucl. Med. Mol. Imaging* **2018**, *45*, 1329–1334.

(51) Yadav, M. P.; Ballal, S.; Sahoo, R. K.; Bal, C. Efficacy and Safety of 225Ac-DOTATATE Targeted Alpha Therapy in Metastatic Paragangliomas: A Pilot Study. *Eur. J. Nucl. Med. Mol. Imaging* **2022**, *49*, 1595–1606.

(52) Nakata, N.; Kobashi, N.; Okumura, Y.; Sato, M.; Matono, M.; Otsuki, K.; Tanaka, A.; Hayashi, A. Radiation Dosimetry and Efficacy of an 89Zr/225Ac-Labeled Humanized Anti-MUC5AC Antibody. *Nucl. Med. Biol.* **2022**, *108–109*, 33–43.

(53) Kelly, V. J.; Wu, S.-T.; Gottumukkala, V.; Coelho, R.; Palmer, K.; Nair, S.; Erick, T.; Puri, R.; Ilovich, O.; Mukherjee, P. Preclinical Evaluation of a 111In/225Ac Theranostic Targeting Transformed MUC1 for Triple Negative Breast Cancer. *Theranostics* **2020**, *10*, 6946–6958.